ACS Photonics 5.2 (2018): 406-412

DOI: http://doi.org/10.1021/acsphotonics.7b00846

Multiline operation from a single plasmon-assisted laser

D. Hernández-Pinilla,[1] P. Molina,[1] C. de las Heras,[1] J. Bravo-Abad,[2] L.E. Bausá,[1]and M.O Ramírez[1]

[1]Dept. Física de Materiales and Instituto Nicolás Cabrera, Universidad Autónoma de Madrid, 28049-Madrid, Spain

[2]Dept. Física Teórica de la Materia Condensada and Condensed Matter Physics Center (IFIMAC), Universidad Autónoma de Madrid, 28049-Madrid, Spain

ABSTRACT - The demonstration of plasmon-assisted lasing by associating optical gain media with plasmonic nanostructures has led to a new generation of nanophotonic devices with unprecedented performances. However, despite the variety of designs demonstrated so far, the operation of these systems is in most cases limited to a single output wavelength, and some reports on multiline emission refer to mixing single nanolasers with the subsequent limitation in compactness. Here, we show multiline operation from a single plasmon-assisted nonlinear solid-state laser on which a linear chain of Ag nanoparticles is deposited. The system provides lasing at 1.08 μm, which is self-converted to the visible range through different parametric frequency-mixing processes generated at metal-dielectric interfaces. Near infrared and simultaneously green and tunable blue radiation with a sub-wavelength confinement in the direction perpendicular to the nanoparticle chain, are obtained at room temperature in CW regime. The results demonstrate the possibility of multifunctional operation from a single plasmon-assisted laser, and offer new avenues for the development of highly integrable sources of coherent radiation.

KEYWORDS: Plasmon-assisted nanolaser, Multiline operation, Nonlinear frequency conversion, Nd^{3+} solid-state laser, Ag nanoparticles chain, Second harmonic generation.

Plasmon assisted lasers have emerged as key tools to face the new challenges in nanoscience and nanotechnology. They operate by taking advantage of subwavelength confined light modes, offering inherent benefits over conventional lasers such as a higher energy density and a lasing threshold reduction. Stimulated by the first experimental evidences of nanoscopic lasing in 2009,[1-3] plasmon-assisted lasers have been reported at different emission wavelengths by associating a variety of gain media (semiconductors,[4-9] organic dyes[10-13] or, recently, solid-state lasers[14]) with plasmonic nanostructures. Despite the diversity of designs experimentally demonstrated so far,[15] plasmon-assisted laser operation is mainly limited to a single output frequency. Indeed, some works on multiline emission are based on the mixing of single nanolasers emitting at different wavelengths, which limits their compactness and reproducibility.[16,17] Recently, multi-modal nanolasing from gold NP superlattices associated with a four level gain system has been reported in the spectral region 860-880 nm.[18] However, the availability of multiline emission at different spectral ranges from a single plasmon-assisted laser is highly desirable to extend the potential functionality of this class of systems, and to allow highly integrated and compact reliable devices. In particular, the ability of providing simultaneous coherent radiation at the near infrared region (NIR) and at the green and blue visible spectral regions is relevant to a variety of fields including high resolution multicolor imaging and displays, ultra-extreme sensing, ultra-dense optical circuits or ultrahigh-density data storage.[17, 19-22]

In this work we demonstrate multiline operation from a plasmon-assisted Nd^{3+} based nonlinear solid state gain media. Namely, a Y-cut Nd^{3+} doped periodically poled $MgO:LiNbO_3$ crystal (hereafter Nd^{3+}: LNB) on which plasmonic chains of Ag nanoparticles (NPs) were photo-deposited on the domain wall surfaces, has been used as active medium. Lasing at the nanoscale at 1.08 μm and simultaneously green and tunable blue radiation generated by different nonlinear self-frequency mixing process are demonstrated. The green radiation is

produced by self-frequency doubling (SFD) of the lasing itself, while the blue radiation is achieved by self-frequency sum (SFS) of the laser and the pump radiation. Both display similar subwavelength confined spatial distribution (in the perpendicular direction to the NP chain) than that to the fundamental laser radiation. The system operates in continuous wave (CW) regime and at room temperature.

The association of a Z-cut Nd^{3+} doped $LiNbO_3$ crystal with linear chains of metallic NPs deposited onto the crystal surface perpendicularly to the polar axis has been recently exploited. Due to the localized surface plasmon (LSP) resonances provided by the metallic chains, the enhancement of both Nd^{3+} luminescence and second harmonic generation (SHG) from the $LiNbO_3$ nonlinear crystal were demonstrated.[23] Additionally, taking advantage of the broad radiative modes of the plasmonic chains, which match the optical transitions (absorption and emission) of Nd^{3+} ions, laser operation with subwavelength confinement was achieved at the near infrared region.[14] However, despite of the remarkable improved operation of this system with respect to the counterpart bulk crystal, the reported threshold and slope efficiency values were not suitable enough to generate nonlinear self-frequency conversion processes at nanometric dimensions. Here we go a step further to demonstrate multiline operation by exploiting a different geometrical configuration and crystal composition. To this aim, plasmonic linear chains of Ag NPs were deposited with orientation parallel to the polar axis on a Y-cut periodically poled Nd^{3+}:LNB crystal. This alternative geometrical configuration makes it possible lasing oscillation of the Nd^{3+} Stark transition with the highest stimulated emission cross-section, thus enabling a substantial improvement of the NIR nanolaser performance. By this means, stable nanoscale laser operation at 1085 nm is obtained with a remarkable 3-fold reduction of the pump power at threshold with respect to the previous report.[14] On the other hand, MgO was incorporated into the gain media to reduce the photorefractive damage, which could prevent stable laser action in $LiNbO_3$.[24] As a result, a superior lasing performance at the

NIR was obtained, which allowed the simultaneous generation of several nonlinear self-frequency mixing processes with subwavelength confinement in the direction perpendicular to the chain in the green and blue spectral region.

It should be mentioned that, although laser action and frequency conversion phenomena have been independently demonstrated,[23, 25] the integration of the two processes into a single optically active system has not been reported up to now. The results of this work demonstrate the possibility of multifunctional stable solid-state lasers operating at the subwavelength regime with multiline operation, which constitutes a technological requirement of great interest for highly integrated compact systems and extends the functionality of current nanolaser devices.

$LiNbO_3$ is an anisotropic uniaxial crystal with a three-fold symmetry rotation axis along the z direction (optical *c*-axis). When incorporated into the crystal lattice Nd^{3+} ions are located in Li^+ sites with a C_3 local symmetry. Due to the noninversion symmetry, the optical transitions between the Nd^{3+} Stark sublevels show forced electric dipole character with specific selection rules depending on the relative orientation of the electric field of the light with respect to the *c* symmetry axis. Figure 1a shows the polarized absorption spectra of Nd^{3+} ions in $LiNbO_3$ corresponding to the $^4I_{9/2} \rightarrow {}^4F_{5/2} + {}^2H_{9/2}$ pumping transition for light polarized parallel (π) and perpendicular (σ) to the crystal *c*-axis. The structure in the spectra is related to the Stark splitting of the manifold states due to the crystal field of the $LiNbO_3$ host. Though the observed Stark transitions display different relative intensities, the maximum absorption values are similar for both configurations. Figure 1b depicts the π and σ polarized stimulated emission cross-section spectra associated with the $^4F_{3/2} \rightarrow {}^4I_{11/2}$ optical transition in which laser action is obtained. The π and σ stimulated emission spectra have been obtained from the experimental spontaneous emission spectra $I^{\sigma,\pi}(\lambda)$ according to[26]

$$\sigma_{sem}^{\sigma,\pi} = \frac{3\lambda^5 \beta I^{\sigma,\pi}(\lambda)}{8\pi n_{\sigma,\pi}^2 c \tau_R \int \lambda \left[2I^{\sigma}(\lambda) + I^{\pi}(\lambda)\right] d\lambda} \quad (1)$$

where β corresponds to the branching ratio of the $^4F_{3/2} \rightarrow {}^4I_{11/2}$ transition (β = 0.52)[27], τ_R is the radiative lifetime of the upper $^4F_{3/2}$ metastable state (100 μs)[27], $n_{\sigma,\pi}$ is the refractive index of the crystal for the σ and π polarizations, respectively, which have been obtained from the Sellmeier equation for $MgO:LiNbO_3$,[28] and $I^{\sigma,\pi}$ stands for the intensity of the measured fluorescence signal for σ and π polarizations. As observed, most of the Stark transitions in the spectra exhibit similar stimulated emission cross-section values for both π and σ configurations, with the exception of π-polarized line at 1085 nm (corresponding to the $^4F_{3/2}(R_1) \rightarrow {}^4I_{11/2}(Y_2)$ Stark transition), whose stimulated emission cross-section is significantly larger than that obtained for the σ-lines. This indicates that the spectroscopic features of the Nd^{3+} based gain medium can play a relevant role in the design of plasmon-assisted lasers. Indeed, the adopted geometrical configuration of the hybrid plasmonic/solid state gain medium will determine the character (σ or π) of the optical transition of Nd^{3+} ions that will interact with the LSP resonances supported by the metallic chains. Figure 1c shows the schematics of the two possible configurations on which linear chains of Ag NPs, formed on the domain wall surface, are arranged along two different crystal orientations as imposed by the photo-deposition process. The left scheme corresponds to a Z-cut geometry on which the linear chains of Ag NPs are assembled perpendicularly to the *c* crystal axis. In this configuration, only Nd^{3+} transitions of σ character are present for light beams propagating perpendicular to the crystal surface (electric field of light perpendicular to the *c* axis). However, for a Y-cut geometry (Figure 1c right), π character transitions are also accessible. Moreover, in this configuration the chains of Ag NPs are aligned parallel to the *c*-symmetry axis, and the excitation of the longitudinal radiative modes of the plasmonic chain with light polarized parallel to the chain produces the specific

enhancement of π polarized Nd^{3+} transitions.[29] In this respect, Figure 2 shows the simulated far field extinction (red line) and absorption (black line) spectra of a linear Ag NP chain for both longitudinal and transverse polarizations. As observed, the linear chain of Ag NPs supports an intense and broad longitudinal LSP mode with a dominant radiative character, which extends from the visible to the NIR (centered at around 600 nm) overlapping the relevant Nd^{3+} absorption bands.[23,30] The Figure also shows the cross-sections of the amplitude of the near field distribution at the NP chain mid-plane computed at the Nd^{3+} lasing emission wavelength (1085 nm) for plane waves polarized parallel and perpendicular to the chain.

Similar mode profiles to those presented in Figure 2 were previously obtained at the pump wavelength for both parallel and transverse polarizations.[14] For waves polarized parallel to the chain, the optical pump excites a plasmonic resonance characterized by a large electric-field enhancement in-between the NPs. This enhancement is significantly reduced when the system is illuminated by a pump perpendicularly polarized with respect to the chain. This justifies the threshold reduction obtained for the longitudinal polarization. Consequently, in this class of systems, an extended plasmonic mode supported by the chain of NPs is coupled to the optical modes of a macroscopic Fabry-Pérot cavity. In that way, the reduction of the threshold observed in this type of hybrid plasmonic-solid state lasers is produced by the local field enhancement associated to the plasmonic resonance, while the overall laser emission linewidth is governed by the photonic modes supported by macroscopic Fabry-Pérot cavity. Thus, in the Y-cut geometry, the LSP resonance supported by the plasmonic chains allow low threshold lasing oscillation of the highest stimulated emission-cross-section line at 1085 nm in π configuration (parallel to the chain, see Fig. 1b), The obtained lasing spectrum is shown in Figure 1d and is related to the $^4F_{3/2}(R_1) \rightarrow {}^4I_{11/2}(Y_2)$ Stark transition of Nd^{3+}. To analyze the spatial distribution of the plasmon-assisted lasing process, two-dimensional spatially resolved

confocal laser gain images were obtained by integrating the laser intensity when the pump radiation was scanned on a macroscopic area of the hybrid-plasmonic-solid state gain media. The inset in Figure 1d depicts the spatial distribution of the laser intensity around a NPs chain for a pump power density of 15mW/μm^2 (above threshold). As shown, it features subwavelength confinement of lasing in the direction perpendicular to the chain and evidences the substantial threshold reduction with respect to the bare Nd^{3+}:LNB regions of the same crystal. Note that lasing action is only obtained at the immediacy of the metallic chains, reproducing the spatial distribution of the plasmonic arrangements whereas it is absent in the remaining areas of the laser crystal.

To get insight into the lasing behavior of the system, Figure 3a shows the lasing performance obtained in the vicinities of the metallic chains at 1085 nm. The laser oscillates parallel to the metallic chains, along the *c*-crystal axis, in agreement with the π character of the Nd^{3+} involved $^4F_{3/2}(R_1) \rightarrow {}^4I_{11/2}(Y_2)$ transition. The gain curves have been obtained for two different polarizations of the pump beam: parallel (red circles) and perpendicular (blue squares) to the Ag NPs chains. In order to carry out the adequate comparison, the pump wavelength was set at λ_p = 811 nm since, according to the polarized spectra of Figure 1a, at this wavelength, the Nd^{3+} absorption presents similar values for both light polarized parallel or perpendicular to the *c*-axis. As observed, the laser efficiency is similar for both pump polarizations. According to a previously developed model for lasing action in plasmonic systems, the slope efficiency is governed by the temporal and spatial light-confining properties of the modes supported by the plasmonic system. Therefore, it is expected that the laser photons generated by each of the two pump polarizations will couple to the same lasing mode (the plasmonic mode that starts lasing first) making the slope efficiency of the hybrid Ag NP chain/Nd^{3+}:LNB gain system independent of the polarization of the pump field.[31,32] Additionally, it should be noted that the slope efficiency of the laser operation at the nanoscale exceeds by a factor of 7 the one obtained

when lasing the counterpart bulk crystal (Figure 3a black triangles). On the other hand, different lasing threshold values are obtained for the two orthogonal pump polarizations. The lowest threshold value corresponds to the pump beam polarized parallel to the plasmonic linear chain, as expected from the strong polarization character of the longitudinal LSP radiative mode supported by the Ag NPs chain.[30] Figure 3b shows the comparison of the subwavelength laser performance for each one of the two configurations depicted in Figure 1c, namely, Y-cut vs Z-cut configurations. Two main differences are observed. The first one refers to the lasing oscillation wavelengths. In agreement with the cross-section spectra, nanoscale lasing oscillation at 1085 nm (π-line) is easily accessible by means of the Y-cut configuration, whereas in Z-cut nanolasing takes place at 1093nm (σ-line).[14] The other difference is related to the substantial 3-fold reduction of the pump power at threshold obtained for the Y-cut configuration compared to the previously reported for the Z-cut geometry. The physical origin of this remarkable improvement of the threshold value is a consequence of the larger stimulated emission cross-section of the π line at 1085 nm, with respect to the σ line at 1093 oscillating in Z- cut geometry. The emission cross-section has a crucial role in the threshold reduction of the system. In agreement with Figure 1b, the cross-section of the π line at 1085 nm is around 3 times larger than the corresponding to the σ line at 1093, from which lasing at the nanoscale has been previously obtained. Accordingly, a threshold reduction up to a factor of 3 is expected in the Y-cut configuration, which agrees well with the experimentally obtained 3-fold threshold reduction.

Once efficient lasing action has been demonstrated from the hybrid Ag NPs chains/Y-cut Nd^{3+}:LNB system, multiline operation was obtained through different parametric sum-frequency mixing processes, which involve the plasmon-mediated CW laser radiation. Self-frequency conversion processes in bulk configuration has shown to be a valuable approach to generate coherent radiation in different spectral regions.[33] Here, this concept is further extended

to nanometric dimensions. That is, by combining the nonlinear properties of the gain media with the subwavelength confined NIR laser oscillation we show that it is possible to simultaneously generate several self-frequency conversion processes with nanoscopic confined spatial distribution. In particular, in addition the NIR lasing, green and blue radiation spatially confined in the vicinity of the Ag NPs chains are simultaneously obtained by self-frequency conversion of the intracavity lasing at 1085 due to the quadratic nonlinear character of the $LiNbO_3$ crystal. The schematics of the result is sketched in Figure 4a. Green emission at λ_{SFD}= 542 nm is achieved via SFD of the fundamental laser radiation at λ_L=1085 nm. On the other hand, blue radiation in the range λ_{SFD}=464-467 nm is obtained by SFS of the fundamental laser radiation at λ_L= 1085 nm and the pump radiation in the range λ_P= 811- 819 nm.

The nonlinear frequency conversion is supported by the plasmonic behaviour of the NP chain. Recently, it has been reported the second harmonic generation enhancement assisted by similar chains of Ag NPs on $LiNbO_3$ lacking of lasing action (without Nd^{3+} doping),[25] As demonstrated, due to the two-photon character of the nonlinear process, the dominant mechanism for the enhancement of the frequency conversion processes is the confinement and enhancement of the near infrared fundamental electric field (which participates quadratically in the process) at the metal/nonlinear-dielectric interface, which is provided by the metallic chains, as shown in Figure 2b.

Figure 4b shows the spectral distribution of the nanoscopic multiline operation (up to three simultaneous processes) at the immediacy of the metallic chains for a fixed pump wavelength at 811 nm. Here we would like to note that only the NIR line at 1085 nm (the one associated with the stimulated emission) corresponds to a lasing mode. In our experiments, the plasmon-assisted lasing action takes place in a CW operation regime for a single longitudinal mode with a linewidth of about $\Delta\omega_{NIR}$ = 0.5 cm^{-1}, which is consistent with the upper limit for the quality factor of the optical resonator Q = 3.5 x 10^5. The visible radiation at 542 nm and at

around 465 nm (largely spaced from the stimulated emission spectral range of the system) are generated by self-frequency conversion of the intracavity lasing at 1085 nm and do not corresponds to lasing gain modes. As observed in Figure 4b, the lasing output intensity is about four and five orders of magnitude more intense than the green and blue nonlinear radiation, respectively, which could serve as a rough estimation of the nonlinear performance of the device. The results provide the experimental proof of concept of multiline operation from a single plasmon-assisted device. Moreover, they involve monochromatic radiation in three technologically relevant spectral ranges such as blue, green and NIR.

Figure 5a shows the spectrum of the self-frequency doubled green radiation. It is spectrally located at twice the energy of the fundamental laser radiation and presents a linewidth (FWHM) of $\Delta\omega_{SFD} = 1$ cm^{-1}. This value is consistent with the spectral position and linewidth of the fundamental laser radiation of the plasmon-assisted solid state-laser ($\Delta\omega_{NIR} = 0.5$ cm^{-1}). Let us recall that the SFD radiation involves the conversion of two near infrared lasing photons into a single one of double energy, its linewidth defined by $\Delta\omega_{SFD} = 2\Delta\omega_{NIR} \sim 1$ cm^{-1}, in agreement with the experimental results. The obtained linewidth is among the narrowest linewidths reported for a subwavelength confined frequency conversion process. Most of the published works devoted to plasmon enhanced frequency conversion processes employs femtosecond or picosecond pulsed lasers as optical fundamental radiation, as they provide high peak power values to favor the generation of nonlinear processes.[34-36] In our work, the high density of fundamental radiation circulating into the cavity when the system is lasing in the NIR, along with the spatial subwavelength confinement in the direction perpendicular to the chains, allows to achieve the energy density values to make possible the nanoscale frequency conversion in a CW regime.

The SFD operation is achieved with a similar subwavelength confined spatial distribution than the fundamental laser radiation. To prove the spatial confinement, the inset in Figure 5a

shows the spatial distribution of the integrated SFD radiation in the vicinity of one linear metallic chain. Similar to the NIR laser distribution (Figure 1d), the green emitted SFD radiation shows a nanoscopic linear spatial distribution around the linear plasmonic chains.

Figure 5b shows the output power dependence of the SFD radiation as a function of the incident pump power obtained when the pump beam was polarized parallel (red circles) and perpendicularly (blue squares) to the Ag NPs chain. In both cases the SFD intensity exhibits a quadratic dependence with the incident pump power radiation, according to the two photon character of the SFD parametric process. Indeed, from the log-log plot displayed as an inset in Figure 5b, a slope value of around 2 is obtained for the two orthogonal pumping polarizations. The SFD curves show two different threshold values depending on the polarization of the pump beam (parallel or perpendicular to the plasmonic chain). A lower SFD threshold value is obtained when the pump beam is polarized parallel to the Ag NPs chain, in agreement with the threshold behaviour obtained for lasing at 1085 nm, which acts as the fundamental radiation in the frequency conversion process. Additionally, the generated SFD nonlinear radiation oscillates parallel to the plasmonic chains, as the NIR laser oscillation. This feature is consistent with the polarization dependence of the longitudinal plasmonic mode supported by the linear chain.[30]

The generation of blue light was achieved by SFS of the laser radiation of our hybrid plasmonic/nonlinear solid-state gain system and the pump radiation provided by the tunable CW Ti:sapphire laser. In particular, the SFS process involves the pump radiation in the spectral region of the $^4I_{9/2} \rightarrow {}^4F_{5/2} + {}^2H_{9/2}$ Nd^{3+} transition (see Figure 1a) and the laser radiation at 1085 nm. Thus, by tuning the pump radiation across the aforementioned Nd^{3+} transition, it was possible to achieve tunable radiation in the blue region of the electromagnetic spectrum. In our experiments, the pumping wavelength is tuned from 811 nm to 819 nm (π-polarized absorption spectrum) which leads to tunable SFS radiation in the 464-467 nm spectral range following the

spectral distribution intensity of the absorbed pump power (See Figure 6). Similar to the green radiation, the SFS process only takes place in the vicinities of the Ag NPs, where lasing is achieved, and hence, the generated blue radiation is also spatially confined at the nanoscale (see inset in Figure 6a). On the other hand, as in the case of the SFD green radiation, the intensity of the emitted SFS radiation shows a nonlinear variation with the incident pump power and presents a polarization parallel to the Ag nanoparticle chains.

Finally, we would like to mention that due to the rich absorption spectrum of Nd^{3+} ions, lasing can be also obtained by pumping at different optical transitions. Therefore, the possibility of generating nanoscopic radiation in other spectral ranges can be envisaged. For instance, pumping at the $^4I_{9/2} \rightarrow {}^4F_{7/2} + {}^4S_{3/2}$ and $^4I_{9/2} \rightarrow {}^4F_{3/2}$ absorption transitions of Nd^{3+} (centered at around 750nm and 890nm, respectively) would allow visible tunable radiation at around 410 nm and 490 nm, separately.

To summarize, we have demonstrated multiline operation with sub-wavelength confinement in a hybrid plasmonic/nonlinear solid-state gain media. Plasmon-assisted lasing operation in a four level laser scheme was achieved at 1085 nm through the selective coupling of the highest emission cross-section transition of Nd^{3+} with the localized surface plasmon resonances supported by metallic chains of Ag NPs. By this means, the lasing performance in the near infrared region is notably improved with respect to previous reports,[14] making it possible the simultaneous generation of different self-frequency conversion processes at the nanoscale. Namely, by taking advantage of both the NIR lasing and the nonlinear character of the host crystal, we demonstrate the simultaneous generation of blue, green and NIR radiation spatially confined in the vicinity of the metallic Ag NPs chain along the direction perpendicular to the chain. The obtained results allow to extend the inherent advantages of plasmon-assisted solid state lasers (such as chemical and thermal frequency stability) to spectral regions typically covered by semiconductors and organic dyes, being relevant for technological applications in

a diversity of fields such as ultra-high resolution displays, imaging, data storage or ultra-high density optoelectronic circuitry.

MATERIALS AND METHODS

Synthesis and Preparation

A Nd^{3+} and MgO co-doped periodically poled $LiNbO_3$ (Nd^{3+}:LNB) crystal was grown by the off-centered Czochralski technique along the *a*-axis.[37] Nd^{3+} was incorporated in the form of oxide during the growth and its concentration in the crystal was determined by total-reflection X-ray fluorescence to be 0.4 at % relative to Nb^{5+}. To minimize the photorefractive damage, around 5 % MgO was added in the melt. A 0.8 mm thick plate was cut and mechanically polished to laser quality with its main surfaces oriented parallel to the crystallographic c-axis (Y-cut).

The plasmonic chains of Ag NPs were formed on the domain walls surfaces of the Nd^{3+}:LNB crystal by means of a photochemical process. The Y-cut crystal plate was immersed in a 0.01M $AgNO_3$ solution at 65°C and illuminated for 10 min with an UV Mercury pen-lamp (UVP model 11SC-1, emission power 5400 μW cm^{-2}, main line located at 253.6 nm). Details on the procedure can be found elsewhere.[29]

Scanning electron microscope (model Philips XL30 SFEG) was used for the morphological characterization of the photo-deposited plasmonic structures. 5 mm long chains of NPs with nearly spherical shape were formed on the domain surface wall. The NPs showed average diameter close to 50 nm and interspacing distances less than 5 nm.

Spectroscopy and laser experiments

The polarized optical absorption spectra of Nd^{3+}:LNB were obtained by using a Lambda 1050 Perkin Elmer spectrophotometer. Photoluminescence was analyzed in a laser scanning confocal microscope by using a Ti:sapphire laser as excitation source.

For the laser experiments, a Y-cut (7 x 5 x 0.8) mm^3 (length x width x thickness) Nd^{3+}:LNB plate was placed between two plane-parallel mirrors. In Figure 4a, the mirror M1 was highly reflective (R>99.7%) at the laser wavelength (λ_L = 1085nm) and showed transmittances T>95% at the pump wavelength (λ_p=811-819nm), T=40.8% at the SFD wavelength (λ_{SFD}=542.5nm) and T=79.1% at the SFS wavelength (λ_{SFS} around 465nm). The mirror M2 was coated for high reflection at the pump and laser wavelengths, and showed transmittances T=70.2% and T=91.7% at the SFD and SFS wavelengths, respectively.

Two 1 mm thick spacers were placed between the mirrors to avoid the contact with the crystal surface. The system was positioned on a two-axis XY motorized platform with 0.2 µm spatial resolution. A tunable CW Ti:sapphire laser (Spectra Physics) was used as excitation source. The pump beam was focused onto the surface of the crystal by an objective lens (20x) with a numerical aperture NA = 0.45, resulting in a spot diameter of around 2.2 µm onto the sample. Lasing, SFD and SFS radiations, were collected in backscattering geometry with the same objective lens and directed by an optical fiber to a Peltier-cooled Horiba Synapse CCD connected to a Horiba iHR 550 monochromator.

Numerical calculations

Near-field simulations were carried out with a commercial implementation of the finite-element method (COMSOL Multiphysics package). Open space in the simulations was mimicked by using perfectly matched layers and scattering boundary conditions. Periodic boundary conditions were used to simulate the optical response of an infinitely periodic chain of metallic nanoparticles. The dielectric permittivity metallic nanoparticles was modeled

following Ref. 38. A Sellmeier formula was used to model refractive index of the laser crystal.[28] The discretization grids in the simulations were refined until a relative numerical error of less than 1% is achieved in all reported results.

The calculated extinction and absorption cross-section were performed by means of the boundary-element method (BEM).[39,40] In these calculations, we considered a finite set of 15 Ag spherical NPs with diameters of 50 and 70 nm randomly distributed and 2 nm of interspacing distances. Increasing the number of interacting NPs above N=15 does not significantly change the spectral shape of the scattering cross section spectrum, but only its intensity (see details of the dependence with N in the Supplementary Information of Ref. 14). Convergence of the results was achieved with use of 2 discretization points per nm at each interface between different materials.

ACKNOWLEDGMENTS

The authors would like to thank Dr. Christos Tserkezis for his valuable contribution with the calculations of the far field extinction and absorption spectra. This work has been supported by the Spanish Ministry of Economy and Competitiveness (MINECO) under projects MAT2013-43301-R and MAT2016-76106-R, and by Comunidad de Madrid under grant S2013/MIT-2740.

REFERENCES

(1) Oulton, R. F.; Sorger, V. J.; Zentgraf, T.; Ma, R. M.; Gladden, C.; Dai, L.; Bartal, G.; Zhang, X. Plasmon lasers at deep subwavelength scale *Nature* **2009**, *461*, 629-632.

(2) Noginov, M. A.; Zhu, G.; Belgrave, A. M.; Bakker, R.; Shalaev, V. M.; Narimanov, E. E.; Stout, S.; Herz, E.; Suteewong, T.; Wiesner, U. Demonstration of a spaser-based nanolaser *Nature* **2009**, *460*, 1110-1112.

(3) Hill, M. T.; Marell, M.; Leong, E. S. P.; Smalbrugge, B.; Zhu, Y. C.; Sun, M. H.; van Veldhoven, P. J.; Geluk, E. J.; Karouta, F.; Oei, Y. S.; Nötzel, R.; Ning, C. Z.; Smit, M. K. Lasing in metal-insulator-metal sub-wavelength plasmonic waveguides *Opt. Express* **2009**, *17*, 11107−11112.

(4) Ma, R-M.; Oulton, R. F.; Sorger, V. J.; Bartal, G.; Zhang, X. Room-temperature sub-diffraction-limited plasmon laser by total internal reflection *Nat. Mater.* **2011**, *10*, 110-113.

(5) Bermúdez-Ureña, E.; Tutuncuoglu, G.; Cuerda, J.; Smith, C. L. C.; Bravo-Abad, J.; Bozhevolnyi, S. I.; Fontcuberta i Morral, A.; García-Vidal, F. J.; Quidant, R. Plasmonic Waveguide-Integrated Nanowire Laser *Nano Lett.* **2017**, *17*, 747–754.

(6) Chou, Y. H.; Wu, Y. M.; Hong, K. B.; Chou, B. T.; Shih J. H.; Chung, Y. C.; Chen, P. Y.; Lin, T. R.; Lin, C. C.; Lin, S. D.; Lu, T. C. High-Operation-Temperature Plasmonic Nanolasers on Single-Crystalline Aluminum *Nano Lett.* **2016**, *16*, 3179-3186.

(7) Shangjr, G.; Chih-Kang, S. Semiconductor plasmonic nanolasers, current status and perspectives *Rep. Prog. Phys.* **2016**, *79*, 086501.

(8) Sidiropoulos, T. P. H.; Roder, R.; Geburt, S.; Hess, O.; Maier, S. A.; Ronning C.; Oulton, R. F. Ultrafast plasmonic nanowire lasers near the surface plasmon frequency *Nat. Phys.* **2014**, *10*, 870-876.

(9) Ramezani, M.; Halpin, A.; Fernández-Domínguez, A.I.; Feist, J.; Rodriguez, S. R.-K.; Garcia-Vidal, F. J.; Gómez-Rivas, J. Plasmon-exciton-polariton lasing *Optica* **2017**, *4*, 31-37.

(10) Hakala, T. K.; Rekola, H. T.; Väkeväinen, A. I.; Martikainen, J. P.; Nečada, M.; Moilanen, A. J.; Törmä, P. Lasing in dark and bright modes of a finite-sized plasmonic lattice *Nature Commun.* **2017**, *8*, 13687.

(11) Meng, X.; Kildishev, A. V.; Fujita, K.; Tanaka, K.; Shalaev, V. M. Wavelength-Tunable Spasing in the Visible *Nano Lett.* **2013**, *13*, 4106-4112.

(12) Suh, J. Y.; Kim, C. H.; Zhou, W.; Huntington, M. D.; Co, D. T.; Wasielewski, M. R.; Odom, T. W. Plasmonic Bowtie Nanolaser Arrays *Nano Lett.* **2012**, *12*, 5769-5774.

(13) Yang, A.; Hoang, T. B.; Dridi, M.; Deeb, C.; Mikkelsen, M. H.; Schatz, G. C.; Odom, T. W. Real-time tunable lasing from plasmonic nanocavity arrays *Nat. Commun.* **2015**, *6*, 6939.

(14) Molina, P.; Yraola, E.; Ramírez, M. O.; Tserkezis, C.; Plaza J. L.; Aizpurua, J.; Bravo-Abad, J.; Bausá, L. E. Plasmon-Assisted Nd^{3+}-Based Solid-State Nanolaser *Nano Lett.* **2016**, *16*, 895-899.

(15) Hill, M. T.; Gather, M. C. Advances in small lasers *Nat. Photonics* **2014**, *8*, 908-918.

(16) Lu, Y. J.; Wang, C. Y.; Kim, J.; Chen, H. Y.; Lu, M. Y.; Chen, Y. C.; Chang, W. H. ; Chen, L. J. ; Stockman, M. I. ; Shih C. K. ; Gwo, S. All-Color Plasmonic Nanolasers with Ultralow Thresholds, Autotuning Mechanism for Single-Mode Lasing *Nano Lett.* **2014**, *14*, 4381-4388.

(17) Ma, R. M.; Yin, X.; Oulton, R. F.; Sorger, V. J.; Zhang, X. Multiplexed and Electrically Modulated Plasmon Laser Circuit *Nano Lett.* **2012**, *12*, 5396-5402.

(18) Wang, D.; Yang, A.; Wang, W.; Hua, Y.; Schaller, R. D.; Schatz, G. C.; Odom, T. O.; Band-edge engineering for controlled multi-modal nanolasing in plasmonic superlattices *Nat Nanotechnol.* **2017**, 12, 889-894.

(19) Wang, X. Y.; Wang, Y. L.; Wang, S.; Li, B.; Zhang, X. W.; Dai, L.; Ma, R. M. Lasing Enhanced Surface Plasmon Resonance Sensing *Nanophotonics* **2017**, *6*, 472-478.

(20) Ma, R. M.; Ota, S.; Li, Y.; Yang, S.; Zhang, X. Explosives detection in a lasing plasmon nanocavity *Nat. Nanotechnol.* **2014**, *9*, 600-604.

(21) Fang, Y.; Sun, M. Nanoplasmonic waveguides, towards applications in integrated nanophotonic circuits *Light Sci. Appl.* **2015**, *4*, e294.

(22) Ma, R. M.; Oulton, R. F.; Sorger, V. J.; Zhang, X. Plasmon lasers, coherent light source at molecular scales *Laser Photonics Rev.* **2013**, *7*, 1-21.

(23) Yraola, E.; Molina, P.; Plaza, J. L.; Ramírez M. O.; Bausá, L. E. Spontaneous Emission and Nonlinear Response Enhancement by Silver Nanoparticles in a Nd^{3+}-Doped Periodically Poled $LiNbO_3$ Laser Crystal *Adv. Mater.* **2013**, *25*, 910-915.

(24) G. Zhong, G. Jian, J.; Wu, Z. Measurement of optically induced refractive index damage in lithium niobate doped with different concentrations of MgO *J. Opt. Soc. Am.* **1980**, *70*, 631–635.

(25) Gómez-Tornero, A.; Tserkezis, C.; Mateos, L.; Bausá, LE.; Ramírez, M. O. 2D Arrays of Hexagonal Plasmonic Necklaces for Enhanced Second Harmonic Generation *Adv. Mater.* **2017**, *29*, 1605267.

(26) Fan, T. Y.; Cordova-Plaza, A.; Digonnet, M. J. F.; Byer, R. L.; Shaw, H. J. Nd:MgO,:$LiNbO_3$ spectroscopy and laser devices *J. Opt. Soc. Am. B* **1986**, *3*, 140-148.

(27) Burlot, R.; Moncorgé, R.; Manaa, H.; Boulon, G.; Guyot, Y.; Solé, J. G.; Cochet, M. D. Spectroscopic investigation of Nd^{3+} ion in $LiNbO_3$, MgO:$LiNbO_3$ and $LiTaO_3$ single crystals relevant for laser applications *Opt. Mater.* **1996**, *6*, 313-330.

(28) Gayer, O.; Sacks, Z.; Galun, E.; Arie, A. Temperature and wavelength dependent refractive index equations for MgO-doped congruent and stoichiometric $LiNbO_3$ *Appl. Phys. B* **2008**, *91*, 343-348.

(29) Molina, P.; Yraola, E.; Ramírez, M. O.; Plaza J. L.; de las Heras, C.; Bausá, L. E. Selective Plasmon Enhancement of the 1.08 μm Nd^{3+} Laser Stark Transition by Tailoring Ag Nanoparticles Chains on a PPLN Y-cut *Nano Lett.* **2013**, *13*, 4931-4936.

(30) Yraola, E.; Sánchez-García, L.; Tserkezis, C.; Molina, P.; Ramírez, M. O.; Aizpurua, J.; Bausá, L. E. Polarization-selective enhancement of Nd^{3+} photoluminescence assisted by linear chains of silver nanoparticles *J. Lumin.* **2016**, *169*, 569-573.

(31) Cuerda, J.; Rüting, F.; García-Vidal, F. J.; Bravo-Abad, J. Theory of lasing action in plasmonic crystals *Phys. Rev. B* **2015**, *91*, 041118.

(32) Chang, S. W.; Chuang, S. L. Fundamental Formulation for Plasmonic Nanolasers *IEEE J. Quant. Electron.* **2009**, *45*, 1014-1023.

(33) Huang, M.; Chen, Y.; Chen, X. Y.; Huang, Y.; Luo, Z. A. CW blue laser emission by self-sum-frequency-mixing in Nd^{3+},$GdAl_3(BO_3)_4$ crystal *Opt. Commun.* **2002**, *208*, 163-166.

(34) Butet, J.; Brevet, P-F.; Martin, O. J. F. CW blue laser emission by self-sum-frequency-mixing in Nd^{3+},$GdAl_3(BO_3)_4$ crystal *ACS Nano* **2015**, *9*, 10545-10562.

(35) Linnenbank, H.; Grynko, Y.; Forstner, J.; Linden, S. Second harmonic generation spectroscopy on hybrid plasmonic/dielectric nanoantennas *Light Sci. Appl.* **2016**, *5*, e16013.

(36) Kolkowski, R.; Szeszko, J.; Dwir, B.; Kapon, E.; Zyss, J. Non-centrosymmetric plasmonic crystals for second-harmonic generation with controlled anisotropy and enhancement *Laser Photonics Rev.* **2016**, *10*, 287-298.

(37) Ming, N. B.; Hong, J. F.; Feng, D. The growth striations and ferroelectric domain structures in Czochralski-grown $LiNbO_3$ single crystals *J. Mater. Sci.* **1982**, *17*, 1663-1670.

(38) Johnson, P. B.; Christy, R. W. Optical constants of the noble metals. *Phys. Rev. B* **1972**, 6, 4370-4379.

(39) García de Abajo, F. J.; Aizpurua, J. Numerical simulation of electron energy loss near inhomogeneous dielectrics *J. Phys. Rev. B* **1997**, 56, 15873.

(40) García de Abajo, F.J.; Howie, A. Retarded field calculation of electron energy loss in inhomogeneous dielectrics *Phys. Rev. B* **2002**, 65, 115418.

Figure 1

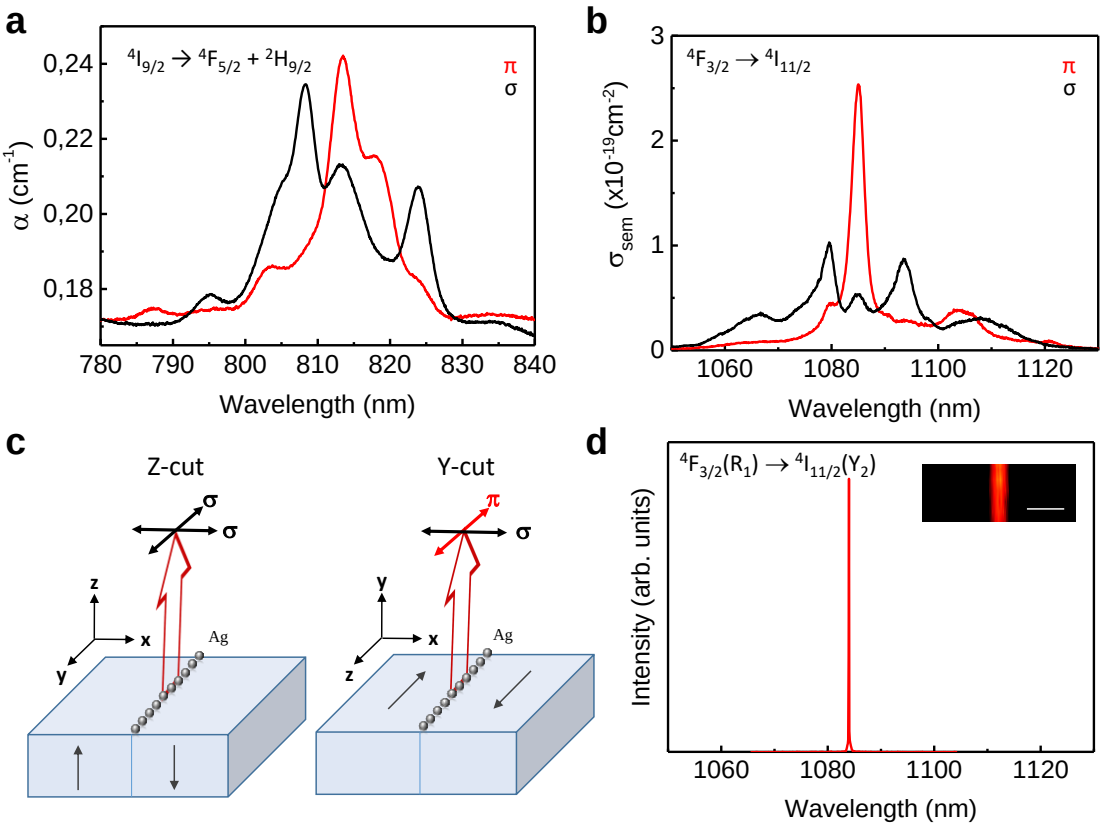

Figure 1. (a) Polarized absorption spectra of Nd^{3+}:LNB in the pump spectral range used in our experiments. The absorption corresponds to the $^4I_{9/2} \rightarrow {}^4F_{5/2} + {}^2H_{9/2}$ transitions of Nd^{3+} ions in π and σ configurations (electric field of the light parallel and perpendicular to the *c* axis, respectively). (b) Polarized stimulated emission cross-section spectra associated with the $^4F_{3/2} \rightarrow {}^4I_{11/2}$ transition of Nd^{3+} ion in π and σ configurations. (c) Schematics of the two possible geometric configurations of the gain medium: Z- and Y-cut Nd^{3+}:LNB crystal on which linear chains of Ag NPs, formed on a domain wall surface, are arranged perpendicularly and parallel to the *c* crystal axis, respectively. (d) Lasing spectrum corresponding to the $^4F_{3/2}(R_1) \rightarrow {}^4I_{11/2}(Y_2)$ Stark transition at λ_e=1085nm. The inset shows the spatially resolved laser gain image obtained by integrating the laser intensity when the pump radiation is scanned on an area containing one single Ag nanoparticle chain. Scale bar corresponds to 2 μm.

Figure 2

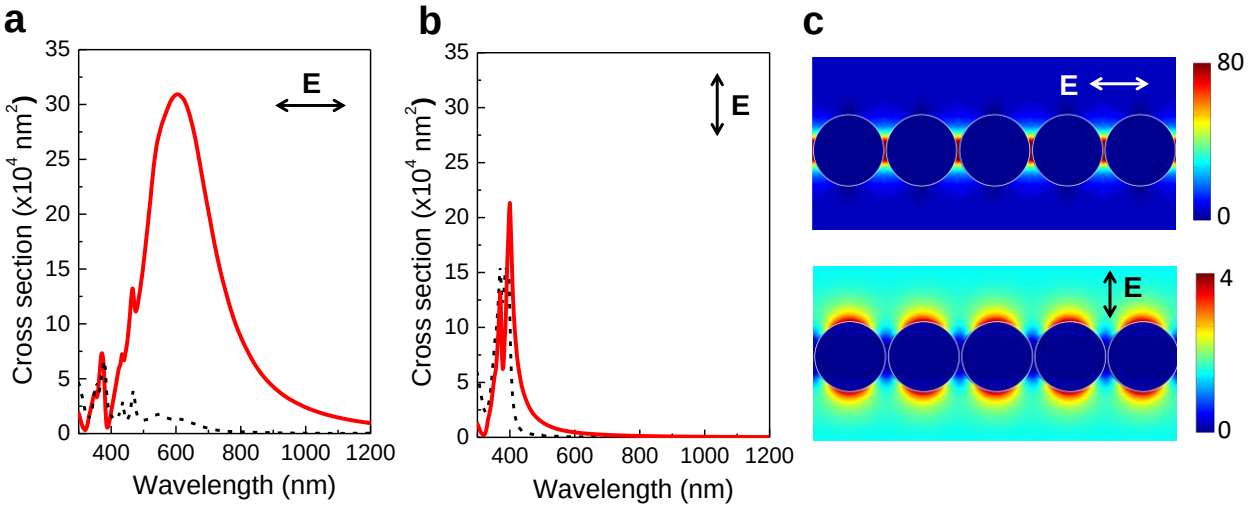

Figure 2. Simulations of the far-field extinction (red) and absorption (dashed black) spectra of a chain of 15 Ag NPs (see Methods) for a wave plane polarized (a) parallel and (b) perpendicular to the chain axis. (c) Distribution of near field amplitudes at the NP chain mid-plane computed at λ = 1085 nm for waves polarized parallel (top) and perpendicular (bottom) to the Ag NP chain.

Figure 3

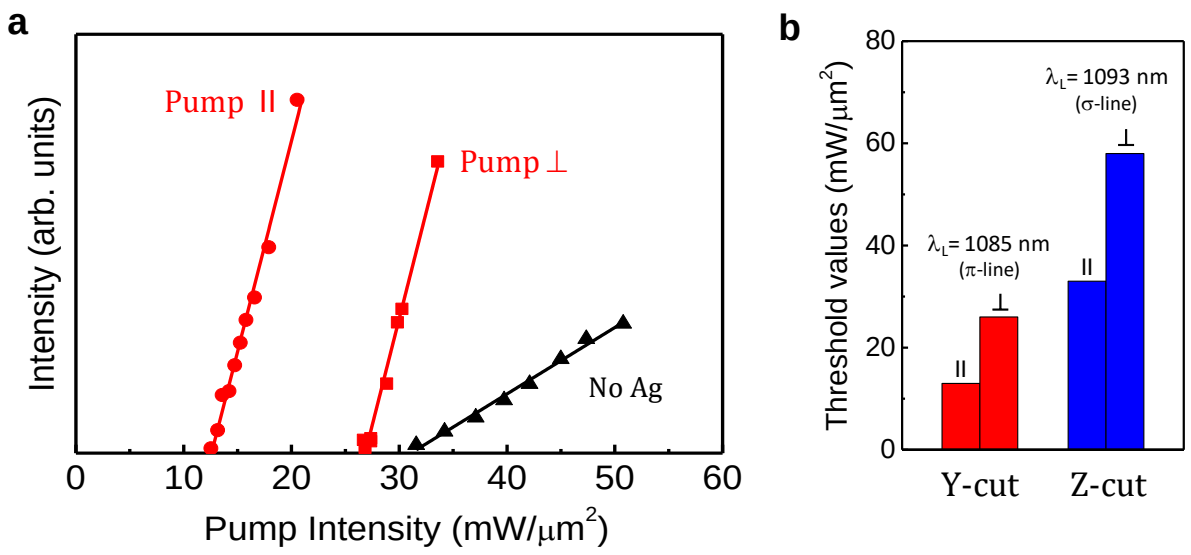

Figure 3. (a) Input-output lasing curves for pump beams polarized parallel (red circles) and perpendicular (red squares) to the Ag NPs chains. The laser performance of the corresponding bulk Nd^{3+}:LNB crystal is also shown (black triangles). (b) Comparison of the laser threshold values obtained in Y-cut and Z-cut configuration (the latter values are obtained from ref.14).

Figure 4

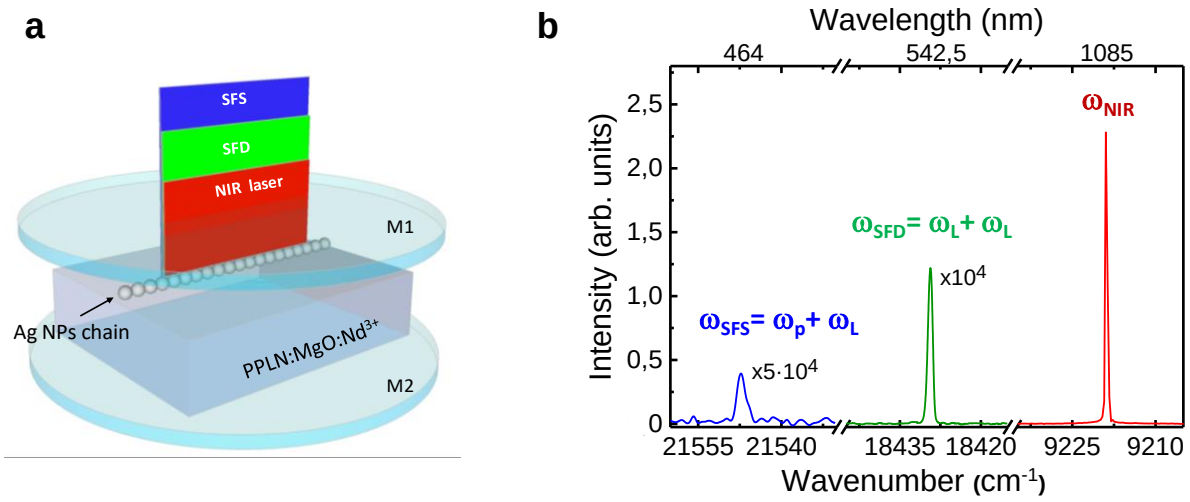

Figure 4. (a) Schematics of the generated nanoscaled confined radiation at the surroundings of a single Ag NPs chain. Lasing features subwavelength confinement in the direction perpendicular to the NP chain. It occurs in a plane perpendicular to the crystal face as imposed by both the 1D NP chain and the Fabry-Pérot resonator. The scheme shows the concurrent emission of lasing, SFD green and SFS blue radiation. The distance between the mirror M1 and M2 is 1 mm. The length of the Ag NP chain illuminated by the pump beam is 2,2 μm. The width of the Ag chain is around 50 nm and the crystal thickness is 800 μm. (b) Spectral distribution of the multiline emission at frequencies ω_L (lasing), $\omega_{SFD} = 2\omega_L$ (SFD), and $\omega_{SFS} = \omega_L + \omega_p$ (SFS).

Figure 5

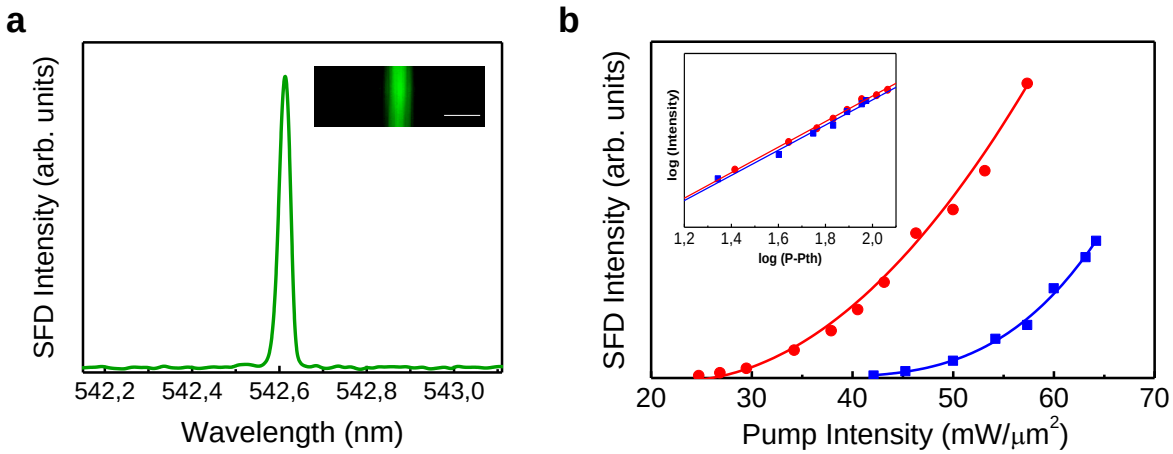

Figure 5. (a) Spectral distribution of the SFD of the nanoscopic NIR lasing at 1085 nm. The inset shows the spatial distribution of the SFD signal obtained around one single Ag NPs chain. The scale bar corresponds to 2 μm. (b) SFD intensity as a function of the pump power for pump polarizations paralell (red circles) and perpendicular (blue squares) to the plasmonic Ag NPs chains. The inset depicts the SFD intensity vs pump power in a log-log representation to evidence the quadratic character of the two photon process. The slope values are 2.12 ± 0.05 and 2.09 ± 0.05 for pump polarization parallel and perpendicular to the Ag NPs chain, respectively.

Figure 6

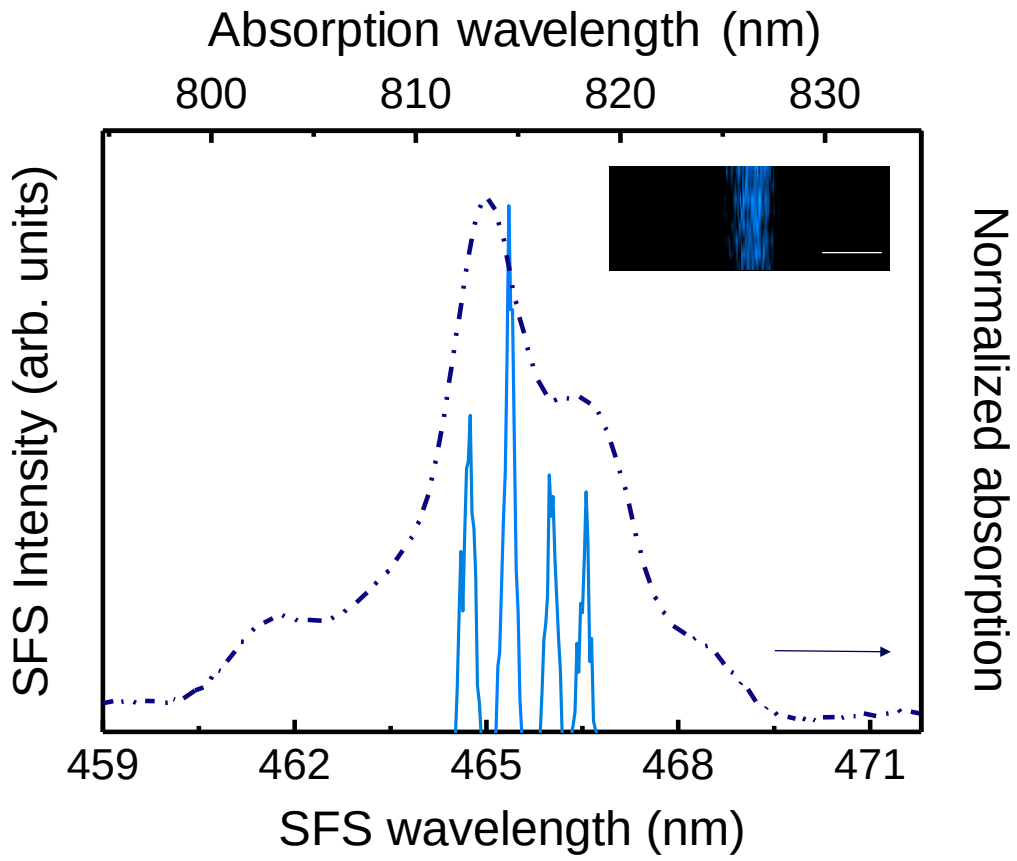

Figure 6. Spectral tunability range obtained by SFS of the fundamental laser radiation at λ_L= 1085 nm and the pump radiation in the range λ_P= 811 - 819 nm. The SFS process involves the $^4I_{9/2} \rightarrow {}^4F_{5/2} + {}^2H_{9/2}$ absorption transition of Nd^{3+} ions in $LiNbO_3$ (dash dotted line). The inset shows the spatially resolved confocal image obtained by integrating the SFS signal around one single Ag NPs chain. The scale bar corresponds to 2 µm.

"For Table of Contents Use Only"

Multiline operation from a single plasmon-assisted laser

D. Hernández-Pinilla,[1] P. Molina,[1] C. de las Heras,[1] J. Bravo-Abad,[2] L.E. Bausá,[1]and M.O Ramírez[1]

[1]Dept. Física de Materiales and Instituto Nicolás Cabrera, Universidad Autónoma de Madrid, 28049-Madrid, Spain

[2]Dept. Física Teórica de la Materia Condensada and Condensed Matter Physics Center (IFIMAC), Universidad Autónoma de Madrid, 28049-Madrid, Spain

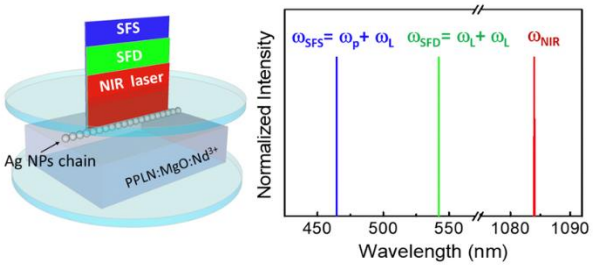

The demonstration of plasmon-assisted lasing by associating optical gain media with plasmonic nanostructures has led to a new generation of nanophotonic devices with unprecedented performances. However, despite the variety of designs demonstrated so far, the operation of these systems is in most cases limited to a single output wavelength, and some reports on multiline emission refer to mixing single nanolasers with the subsequent limitation in compactness. Here, we show multiline operation from a single plasmon-assisted nonlinear solid-state laser on which a linear chain of Ag nanoparticles is deposited has been deposited. The system provides lasing at 1.08 µm, which is self-converted to the visible range through different parametric frequency-mixing processes generated at metal-dielectric interfaces. Near infrared and simultaneously green and tunable blue radiation with a sub-wavelength confinement in the direction perpendicular to the nanoparticle chain, are obtained at room temperature in CW regime. The results demonstrate the possibility of multifunctional operation from a single plasmon-assisted laser, and offer new avenues for the development of highly integrable sources of coherent radiation.